Research Article | Vol. 31, No. 10 / 8 May 2023 / Optics Express 15301
Optics EXPRESS

Sparse interleaved sampling for high resolution focal construct geometry X-ray tomography

J. P. O. Evans,[1,*] F. Elarnaut,[1] D. Downes,[1] W. K. Lee,[1] E. L. Arnold,[2] and K. Rogers[2]

[1]Imaging Science Group, Rosalind Franklin Building, Clifton, Nottingham Trent University, Nottingham, UK
[2]Cranfield Forensic Institute, Cranfield University, Shrivenham, Swindon, UK
[*]paul.evans@ntu.ac.uk

Abstract: We demonstrate interleaved sampling by multiplexing conical subshells within the tomosynthesis and raster scanning a phantom through a 150 kV shell X-ray beam. Each view comprises pixels sampled on a regular 1 mm grid, which is then upscaled by padding with null pixels before tomosynthesis. We show that upscaled views comprising 1% sample pixels and 99% null pixels increase the contrast transfer function (CTF) computed from constructed optical sections from approximately 0.6 line pairs/mm to 3 line pairs/mm. The driver of our method is to complement work concerning the application of conical shell beams to the measurement of diffracted photons for materials identification. Our approach is relevant to time-critical, and dose-sensitive analytical scanning applications in security screening, process control and medical imaging.

1. Introduction

Three-dimensional X-ray imaging is an important tool for the evaluation and characterization of internal object structures across a broad range of application areas including industrial inspection [1–3], medical diagnostics [4,5] and security screening [6–9]. At sub-mm length scales, the use of hard X-rays is often a prerequisite. Modalities including computed tomography (CT) [5], tomosynthesis [4], laminography [10], and phase contrast imaging [11] have developed into screening tools where mass attenuation coefficients and refractive indices provide the contrast mechanisms, respectively. Also, recent advances in multi-emitter switched X-ray sources [12,13] provide sequenced firing that can replace mechanical scanning, which is an important driver of our ongoing effort concerning rapid data acquisition.

Our work concerns the detection of shape-based threats such as guns, knives/sharps, and improvised explosive devices (IEDs) in the screening of air passenger luggage. For example, IEDs can be detected via shape signatures associated with detonators and timers including electronic components and fine wires. However, the bulk charge component of an IED may be fashioned from a wide range of highly shape-variant plastic or homemade explosives including liquids. Such materials, including illicit drugs such as fentanyl, require material-specific information for enhanced false-alarm resolution [7,14,15]. Methods including coded aperture coherent scatter tomography [16] and hyperspectral X-ray computed tomography [17] show promise but significant challenges remain in dealing with spatially complex scenes in real-world screening applications. We have previously reported (see Section 2.1) materials characterization using conical shell X-ray diffraction (XRD) applied to tomography. A combined high-energy XRD and high-resolution absorption contrast probe [18] promises a cost-effective solution that would increase the throughput of carry-on and checked luggage at inspection points. This development would be a disruptive advance for security screening applications.

#484008 https://doi.org/10.1364/OE.484008
Journal © 2023 Received 21 Dec 2022; revised 21 Feb 2023; accepted 27 Feb 2023; published 24 Apr 2023

Optics EXPRESS

While our approach uses sparse views it is significantly different from compressed or sparse sensing involving solutions to underdetermined linear systems [19–21]. For example, we do not make assumptions concerning the 'sparsity' or degree of 'compressibility' [22] of our sampled data but, in contrast, we apply a deterministic algorithm to construct optical sections. Such an approach does not require the setting of convergence criteria that are inherent in iterative methods. It also does not require interpolation or image cross-correlation as used in super-resolution [23]. Instead, our new method is entirely deterministic.

In this paper, we report an advance in shell beam tomosynthesis that demonstrates a fivefold increase in the contrast transfer function (CTF) in comparison with prior methods. The new and central novelty is the sampling of concentric conical subshells (see Fig. 1(b)) to composite a series of highly sparse radially offset projection data from a relatively coarse sampling grid i.e., the treatment of the subshell views within the novel tomosynthesis. Data acquired from each sampling point on a subshell is positioned periodically within an upscaled grid that is subsequently padded with nulls. For example, each resultant image may comprise 1% samples and 99% nulls. The novel tomosynthesis focuses and 'tracks' the axially dependent interleaved patterns of contributing pixels, from each sampling point on every subshell, and applies the appropriate weighting factors in the construction of optical sections.

This initial paper reports the proof-of-concept of the novel method and the spatiotemporal analysis of experiment results, rather than the optimization of data acquisition and scan speed. Our work is organized as follows. Section 2 presents the theoretical background; the methods (including our new imaging technique) and describes the experiment conditions. Section 3 presents our experimental results and discussion. Section 4 summarizes our conclusions, the implications of our findings and the future direction of the work.

2. Methods

2.1. Theory background

We have developed a body of work termed focal construct geometry (FCG) [24], which exploits shell beam X-ray probes for rapid, sub-second [25], structural or molecular analysis of samples. In comparison with conventional beam topologies such as a pencil or line beam, the focal construct method uses an extended annular measurement gauge volume to produce relatively high-intensity focal spots [26] and caustics in the diffracted flux [27]. The focal construct approach has been applied in angular dispersive mode [26,28], and energy dispersive mode [25,29], used to identify liquid samples [30], and shown to deal favorably with non-ideal samples [31] (i.e., in which scattering distributions are adversely affected by large grain size and crystallographic textures [32]). We have also demonstrated focal construct XRD in reflection mode [33]. Imaging methods employing focal construct principles include angular-dispersive XRD tomography [27], energy dispersive tomography [34], absorption contrast tomography [35,36], and more recently, combined absorption and XRD tomography [18] using a single shell beam. This paper reports a new complementary method in which each annular projection is sampled and processed as a set of multiplexed subshells. The pixel data are null padded and normalized via novel tomosynthesis to produce high-resolution optical sections.

2.2. New interleaved-theoretic method

Our technique aims to produce high-resolution optical sections constructed from highly sparse oblique or inclined parallel projections. The data is collected from a series of annular projections during a two-axis translational scan of the phantom through a conical shell beam [35], see Fig. 1(a). A specific detection point within the incident annular beam when sampled periodically will produce a pixel stream that can be composited to form an oblique projection $M_{xy}(r, \gamma)$ comprising pixels $M_p(r, \gamma, x_M, y_M)$; where r is the radius measured in pixels to the detection point

Optics EXPRESS

at the azimuth γ. As we have previously reported [35,36] a circular path of such points enables a series of oblique projections to be recovered with an angular separation $a = 2\pi/v$ where v is the total number of circumferential sampling positions. It follows that the azimuth of a given oblique projection may be expressed as

$$\gamma(j) = aj \tag{1}$$

where $j = 0, 1, 2, 3, \ldots . v - 1$.

In our new approach, we model the incident conical shell beam as a tightly packed series of concentric subshell beams, see Fig. 1(b). This is a convenient construct because each oblique projection $M_{xy}(r, \gamma)$ that composes a subshell series $M_{\gamma xy}(r)$ (i.e., at a fixed radial magnitude) undergoes the same magnitude digital radial shift in the tomosynthesis. We assume here that the X-ray focal spot dimensions are much less than the minimum detectable increment on the detection surface δr.

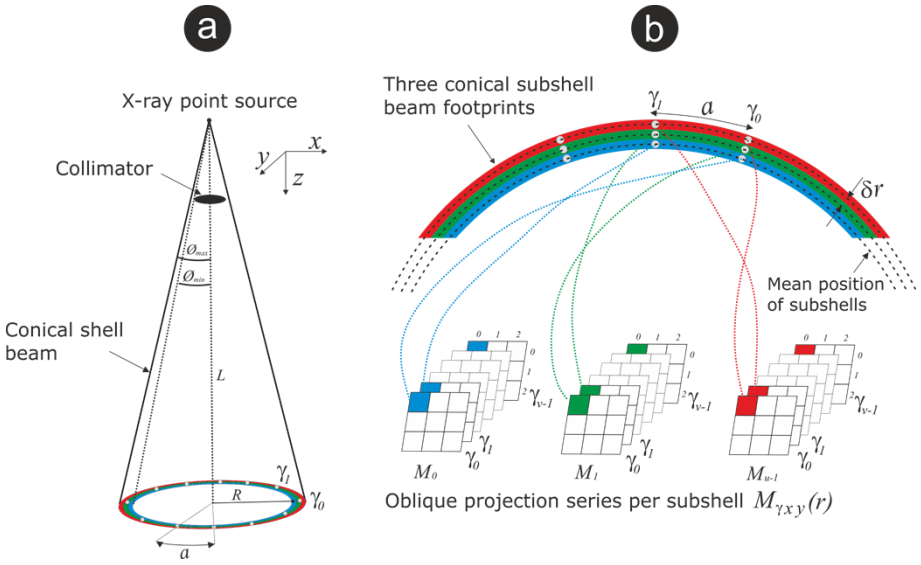

Fig. 1. (a) A schematic of a conical shell X-ray beam and incident annular footprint on a detection surface; where $\phi_{\max/\min}$ are the outer/inner half-opening angles of the beam envelope, γ is the azimuth and 'a' is the incremental change in azimuth, L is the separation between the point source and the detection pane, and R is the mean radius of the innermost (blue) subshell on the detection plane. A phantom is raster scanned (x,y) through the beam (or equivalently vice versa) to enable a series of annular projections to be recorded. By registering the pixels sampled at their respective (x,y) positions in the scan, for a given azimuth and radial magnitude, an oblique (or inclined parallel) projection can be composited. Fig. (b) A schematic of an annular sector of the beam footprint (bounded by the inner and outer shell beam envelope) on the detection surface. In this example, the system is modelled as a series of three 'color coded' discrete concentric subshells centered on their mean radii (up to eight subshells are multiplexed during tomosynthesis in the experiments in this paper). The separation between a successive pair of radii is the minimum detectable radial increment δr. Thus, three different projection series $M_{\gamma xy}(r)$ are collected from around their respective subshells. A specific series requires a constant magnitude of radial shift to effect a given axial focal plane position and requires appropriate multiplexing in the tomosynthesis.

In addition, we consider the original physical sampling positions as nodes on a higher resolution or upscaled uniform rectilinear grid. To 'fill in' the unused virtual sampling positions in the production of oblique projections requires interleaving sample pixels with null pixels. The pattern

Optics EXPRESS

of interleaving is represented in an upscaled null padded sample map $\rho'(x, y)$. The construction of such maps is central to our new method and required for tracking and normalization of sample contributions on a pixel-by-pixel basis at each different axial focal plane position. To better understand the mapping process, we first consider the discrete axial scan-step S implemented in the physical sampling grid shown in Fig. 2(a), which is upscaled by introducing virtual or null sample positions shown in (b); where physical sampling positions are represented by pixel centroids in (c) and (d), respectively.

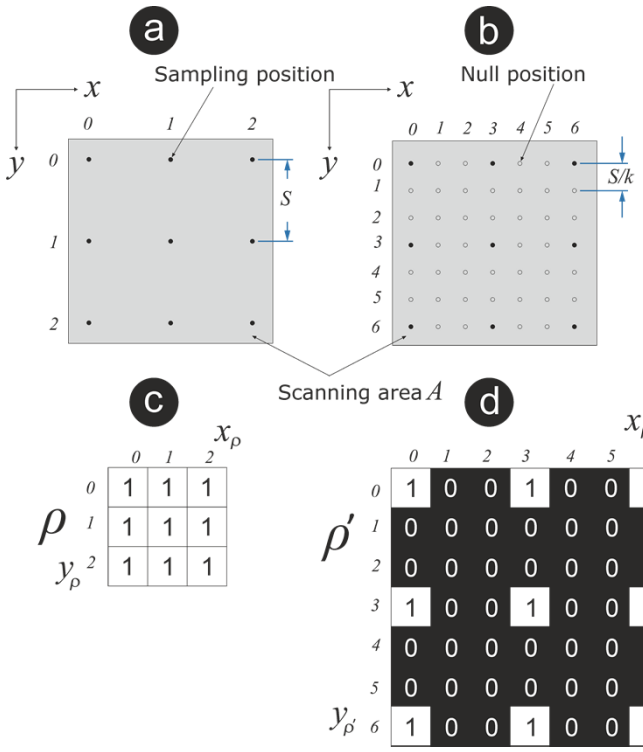

Fig. 2. (a) Scanned area A showing 3×3 sampling positions with a step size of S. (b) Upscaled axial resolution δS for $k = 3$ showing a combination of real and null sampling points. (c) Original digital map ρ and, (d) upscaled 7×7 interleaved map ρ'.

The virtual scan step size δS is chosen according to

$$\delta S = \frac{S}{k} : k \in \mathbb{N}_{\geq 1} \tag{2}$$

where k is termed the upscaling factor and parameterizes the axial resolution upscaling, where unity indicates no upscaling. It follows that in the general case sampling comprising NM nodes then the ratio of the total number of samples to the samples and nulls composing the upscaled grid is given by $\eta = NM/[(kN - k + 1)(kM - k + 1)]$ termed the upscaling ratio. It can be appreciated that for a square grid where $(N \equiv M) >> k$ then $\eta \approx 1/k^2$. We remember here that the dimension of the scanned area A and the physical locations of the real sampling points are fixed, and the upscaling does not involve interpolation nor any change to the measurements collected during the scan. In general, an upscaled interleaved map $\rho'(x, y)$ see Fig. 2. (d), with dimensions, $(kN - k + 1)(kM - k + 1)$ is obtained by transforming the original map ρ by the following

$$\rho'(x_{\rho'} y_{\rho'}) = \begin{cases} 1 \text{ if } x_{\rho'} = k x_{\rho} : x_{\rho} \in \mathbb{Z}_N \wedge y_{\rho'} = k y_{\rho} : y_{\rho} \in \mathbb{Z}_M \\ 0 \text{ otherwise} \end{cases} \tag{3}$$

Optics EXPRESS

Thus, $\rho(x, y)$ is transformed into an upscaled map, where $\rho'(x, y) = f(\rho, k)$, and $(k - 1)$ contiguous columns and rows of null elements are interleaved between NM unity values representing the real sampling positions. This padding process is also applied to all oblique projections M specifically, a padded projection $P_{xy}(r, \gamma)$ is created by replacing unity values in the map $\rho'(x, y)$ with corresponding measured values; all such padded projections are denoted by P.

Constructing optical sections requires an appropriate shift algorithm to multiplex the subshell samples. To register a sequence of padded oblique images $P_{\gamma xy}(r)$, produced using a circular path of scanned sample points, at a specific axial focal plane position requires that each image $P_{xy}(r, \gamma)$ be translated a constant radial distance r at its respective azimuth γ. Thus, image centers (x_P, y_P) in sequence $P_{\gamma xy}(r)$ are shifted to produce a new relative registration (x_D, y_D) in the new image sequence $D_{\gamma xy}(r)$. And for each pixel $D_p(r, \gamma, x_D, y_D)$ in the image $D_{xy}(r, \gamma)$ of the image sequence $D_{\gamma xy}(r)$ of a nested 'concentric' collection of sequences D

$$D_p(r, \gamma, x_D, y_D) \equiv P_p(r, \gamma, x_P, y_P) \tag{4}$$

and, for an axial focal plane position at a distance z from the point source

$$\begin{aligned} x_D &= \lfloor x_P + r(i) \cos\gamma + 0.5 \rfloor \\ y_D &= \lfloor y_P + r(i) \sin\gamma + 0.5 \rfloor \end{aligned} \tag{5}$$

the radial pixel shift $r(i)$ applied to the collection of 'concentric subshell' sequences D

$$r(i) = \frac{z(R + i\delta r)}{L\delta S} \tag{6}$$

where $r(i)$ is a real positive number with a fractional part, which is indexed by $i = 0, 1, 2, 3, \ldots .u-1$, for a given axial focal plane z position, δr is the minimum detectable radial increment on the detection plane, R is the minimum mean shell radius, and L is the separation between the detection plane and the point source. A shift value $r(i)$ of zero corresponds to an axial focal plane position at the source whereas the maximum shift value corresponds to the detection plane, which is a function of the geometric configuration under consideration. The maximum total number of shells is given by $u = \lfloor(\Delta r/\delta r)\rfloor$ where the radial separation between the minimum and the maximum shell radius of the incident annular beam is $\Delta r = f(L, \phi_{\min}, \phi_{\max}) \approx u\delta r$.

Constructing a normalized optical section requires that the sample pixel contributions be mapped for a given axial focal plane position to account for null pixels in the tomosynthesis. Each different axial focal plane position has a unique normalization map ω_z generated by replacing each (shifted) image composing $D_{\gamma xy}(r)$ with an equally shifted map ρ' following

$$\omega_z = \sum_{i=0}^{u-1} \sum_{j=0}^{v-1} \rho'(r(i), \gamma(j)) \tag{7}$$

and contributions from all projections of the multiplexed subshells, collected from different sampling points within the annular region are represented by their corresponding map. Through similar considerations, a set of summed padded oblique projections G_z for r are given by

$$G_z = \sum_{i=0}^{u-1} \sum_{j=0}^{v-1} D_{xy}(r(i), \gamma(j)). \tag{8}$$

The associated ω_z contribution map is applied to construct a normalized digital optical section T_z

$$T_z(x, y) = \frac{G_z(x, y)}{\omega_z(x, y)} \tag{9}$$

Optics EXPRESS

where each successive section is normalized as a $f(z)$. It should be noted that the normalized digital optical section T_z, via the application of Eqs. (8,9), reduces non-systematic measurement noise in proportion to ω_z.

2.3. Experiment setup

A bespoke X-ray chamber containing an X-ray generator, image intensifier, and movement stage was used to collect the experiment data. The cone shell projections were produced using a microfocus (tungsten anode) X-ray source manufactured by Hamamatsu; model L12161-07, with a focal spot size of ~7 µm, with the accelerating voltage set to 150 kV and tube current 66 µA. The phantoms were placed on a carbon fiber table attached to a 3-axis movement stage to effect an in-plane (x,y) discretised raster scan. The projections were sampled and quantized via an image intensifier with a 160 mm diameter (useful entrance field) CsI phosphor input screen manufactured by Siemens; model HIDEQ 33-4 ISX, optically coupled to a Videomed-XR2 GigE camera with 1 k x 1 k pixels, 16-bit resolution, running at 30 frames/s. To capture annular images of appropriate contrast and brightness an exposure of 66 µAs was implemented by averaging 30 frames per stationary scan point, yielding a total image acquisition time of ~5.5 hours for 141^2 scan points used in our experiments. An additional period of ~2.3 hours was required for the movement between sample points including a ~50 s flyback per scan line (to counter any backlash positioning error in the movement stage). Thus, the total data acquisition time was ~7.8 hours (for experiment one and experiment two, described in the following text). Note that these proof of principle experiments were designed to test the (spatiotemporal) theoretic basis of our novel method rather than optimize the speed of data acquisition, which is a separate task. A pathway to reducing the acquisition time is presented briefly as future work in Section 4.

In the first experiment, a 50 mm square line-pair test pattern supporting 0.6–3.4 line pairs per mm (LP/mm) manufactured by Leeds Test Objects (Type 41-005) [37] was scanned to provide the data for a comparative analysis of the CTF under different upscaling and subshell parameterizations. Conical shell digital projections were collected from an annular ROI corresponding to a min/max half shell opening angle of $\phi_0 = 9.97°$ and $\phi_{u-1} = 10.10°$, respectively. The separation between the source and the input window of the image intensifier was 404 mm, and the distance from the X-ray source to the phantom was 147 mm. The test pattern was raster scanned through 141 positions along the x-axis, and the y-axis, in steps of $S = 1.0$ mm, forming a 140 mm square grid. These experimental parameters were also applied to the analysis of fill factor and interleaved maps presented in Section 3.1.

In the second experiment, a phantom featuring objects with irregular and complex morphology was designed to be representative of a real-life application i.e., a core section through 'luggage' that emulates a security screening scenario, see Fig. 3.

To accommodate the ~35 cm height (z-axis) of the phantom in the inspection space the separation between the point source and the image intensifier input window was increased to 491 mm and the distance from the X-ray source to the translation table was reduced to 139 mm. Thus, the digital projections collected from the annular ROI subtended reduced min/max half opening angles $\phi_0 = 8.56°$ and $\phi_{u-1} = 8.68°$, respectively. As in experiment one, the phantom pattern was raster scanned through 141 positions along the x-axis, and the y-axis, in steps of $S = 1.0$ mm, forming a 140 mm square grid.

Optics EXPRESS

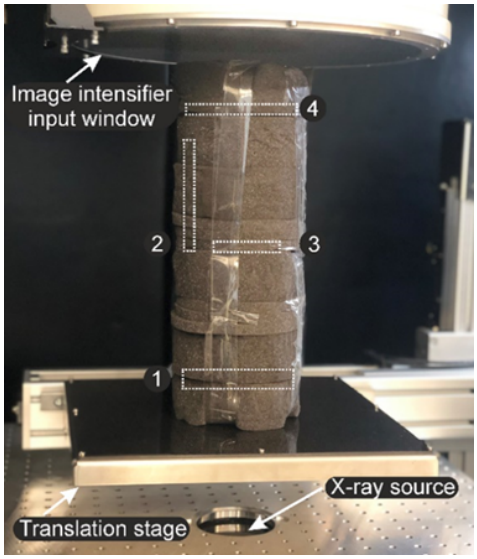

Fig. 3. Luggage core phantom mounted on the carbon fiber translation table in the X-ray inspection chamber. Objects 1-4 are embedded in radiotranslucent foam at the positions indicated. The approximate distance along the z-axis (origin at the point source) to the nearest feature on each object is (1) Mobile Phone ~170 mm, (2) Plastic marker pen ~305 mm, (3) Printed circuit board ~305 mm, and (4) NTU letters in tightly coiled copper wire, two steel washers connected via a fine wire, ~419 mm. The separation between the source and the image intensifier input window is ~491 mm.

3. Results and discussion

3.1. Fill factor and interleaved maps

The presence of nulls in an optical section can be identified by examination of the corresponding contribution map ω_z, and expressed as a fill factor (FF). The FF is defined as the ratio of pixels with valid data to all pixels (both those with valid data and null valid data) composing an optical section; valid data is that which originates from a physical detector signal. Thus, a section containing zero nulls has a FF of unity. In the following discussion, it is convenient to show the axial dependency of FF via FF (%), noting that this is a focal plane position characteristic.

Contribution map sequences ω were generated by applying Eqs. (1)-(7) to the 'first experiment' parameters in Section 2.3. The characteristics plotted in Fig. 4 compare maps generated with upscaling factors, respectively, $k = 2, k = 5$, and $k = 10$ each with a single digital subshell $i = 0$. The characteristic plotted in Fig. 5 compares a fixed upscaling factor $k = 10$ with a single subshell $i = 0$, and with eight multiplexed subshells $u = 8$ (indexed by $i = 0, 1, 2, 3, \ldots .u - 1$ in Eqs. (5) and (6).

Optics EXPRESS

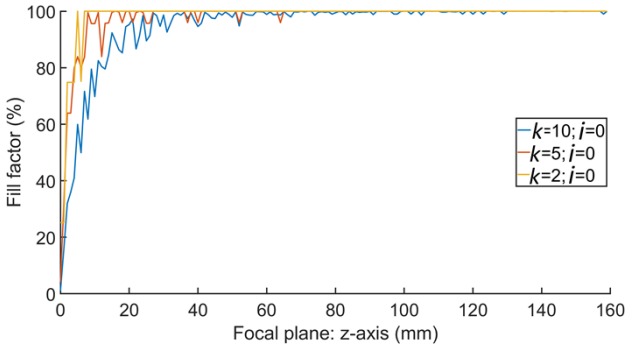

Fig. 4. Fill factor percentage against the axial focal plane position for $N = M = 141$ sampling using a single shell projection $i = 0$. The upscaling factor k, upscaling ratio $\eta \times 100\%$ (intercept), and the total number of pixels composing the optical section $(kN - k + 1)^2$ for each plot respectively are (2, 25.2%, 281^2), (5, 4.0%, 701^2), (10, 1.0%, 1401^2). The range of the z-axis is truncated to highlight initial growth.

The minimum FF is equal to the upscaling ratio $\eta \times 100\%$, as indicated by the intercepts on the plots of Figs. 4 and 5. This occurs because the (hypothetical) axial focal plane at $Z = 0$ is coincident with the source plane. The normalization map $\omega_z : r(i, z = 0) = 0$, see Eqs. (6) and (7), is thus the sum of a perfectly aligned stack of maps ρ', where all contributions condense onto NM nodes to form an image of the relative point source positions required over the raster scan. The value of η recorded in Fig. 4 reduces from 25.2% for $k = 2$ to 1.0% for $k = 10$ as predicted by the theoretic analysis presented in Section 2.2. This result is independent of the total number of subshells u as all contributions from each subshell map to their originating 'point source' position at the source plane. However, increasing the total number of shells from 1 to 8 for a constant value of k increases the total number of sample pixels available in the tomosynthesis by approximately eightfold. The increase in available samples stabilizes the FF at 100% relatively close to the source plane at $z \sim 60$ mm, whereas in the single shell case nulls occur intermittently up to $z \sim 160$ mm, see Fig. 5.

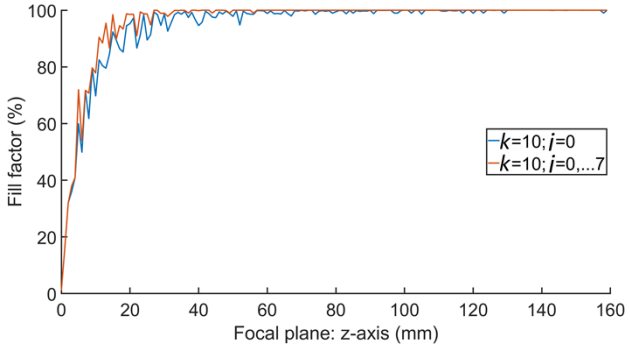

Fig. 5. Fill factor percentage as a function of axial focal plane position for a constant upscaling factor $k = 10$, using a single shell projection $i = 0$, compared with eight combined contiguous shells $i = 0, 1 \ldots 7$.

Each different axial focal plane position requires a unique contribution map for a given upscaling factor k and subshell index i. The example maps shown in Fig. 6 were used in the construction of optical sections shown in Fig. 7. The increase in the total number of contributing

Optics EXPRESS

pixels when increasing from a single shell in comparison with multiplexing eight shells can be appreciated from the color-coded scale in Fig. 6. The density distribution of both maps is similar as they share the same $k = 10$ value.

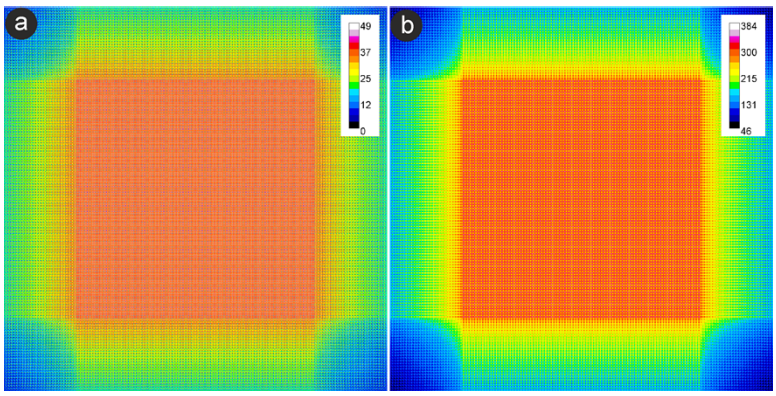

Fig. 6. An example of color-coded contribution maps ω_z each comprising 1401^2 pixels. The color indicates the normalization weightings for an axial focal plane position at z = 147 mm (see Fig. 7) for an upscaling factor $k = 10$, and $N = M = 141$. (a) A contribution map for a single shell $i = 0$ records mean, min and, max values of 28, 0, and 49, respectively. (b) Eight contiguous shells; $i = 0, 1, \ldots 7$ records mean, min and, max contributions of 222, 46, and 384, respectively.

The following Section 3.2 presents a comparative analysis of the reconstructed image parameters including CTF analysis and optical sections from the luggage core phantom.

3.2. CTF analysis

The line-pair test pattern was placed on the inspection table and scanned according to the experimental conditions described in Section 2.3. X-ray measurements were collected and processed according to Eqs. (1)–(9) using eight different subshells, $u = 8$. To conduct a comparative CTF analysis four optical sections were constructed using identical sampled data but different upscaling factors respectively $k = 1, 2, 5, 10$, see Fig. 7. The contrast transfer function $CTF(x) = C(x)/C(0)$ [38] for each orthogonal pair of line-pair patterns was computed and the least favorable response plotted in the CTF graph of Fig. 8. The plots k = 1,2,5 indicate that the relative improvement in CTF was approximately proportional to the upscaling factor and in good agreement with our theory as well as the computed CTFs. Also, the empirical limiting resolutions agreed well with the Nyquist frequency $f_n = k/2S$ predicted by the upscaled sampling rate where k and f_n LP/mm are respectively (1, 0.5), (2, 1), (5, 2.5). However this prediction did not hold for $k = 10$ as the virtual scan step $\delta S = 100$ μm is less than the minimum detectable increment $\delta r \sim 165$ μm. Thus, improvements in the CTF were limited to $k \sim 6$ equating to ~3 LP/mm, which is the native resolution of the detector/source system. The native CTF was calculated independently from a conventional 'solid angle' snapshot of the test phantom using the same experiment rig and X-ray parameters.

Optics EXPRESS

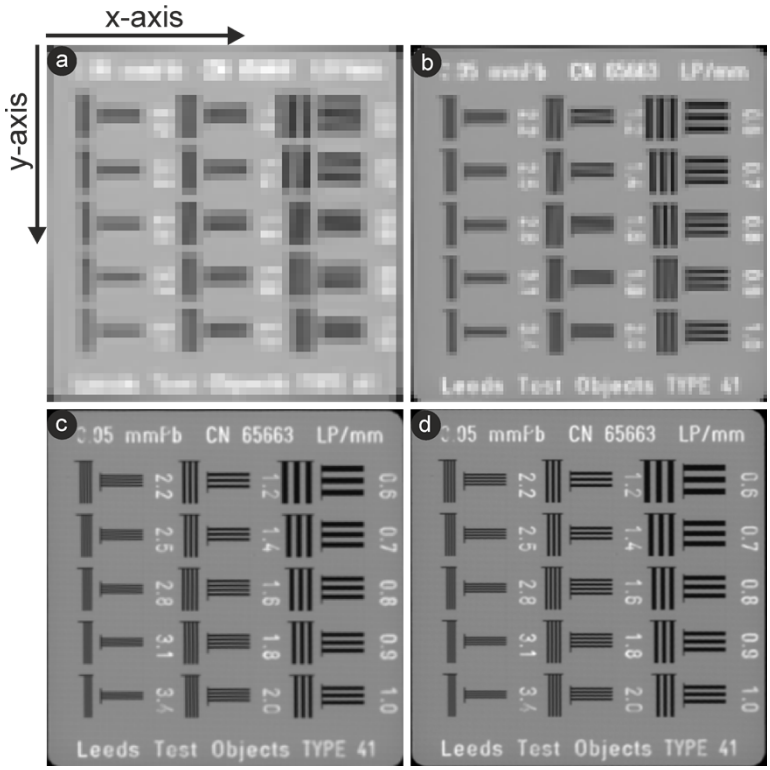

Fig. 7. A montage of four optical sections of the 50 mm square L/P test phantom positioned $z = 147$ mm from the source. Each section has been produced using identical projection data collected from a 140 mm square raster scan (each image of the phantom is cropped to represent ~50 mm square) using eight contiguous shells, $u = 8$ where the upscaling factor k, upscaling ratio $\eta \times 100\%$, and the total number of pixels are as follows. (a) $k = 1$, 100%, 141^2 pixels; (b) $k = 2$, 25.2%, 281^2 pixels; (c) $k = 5$, 4.0%, 701^2 pixels; (d) $k = 10$, 1.0%, 1401^2 pixels.

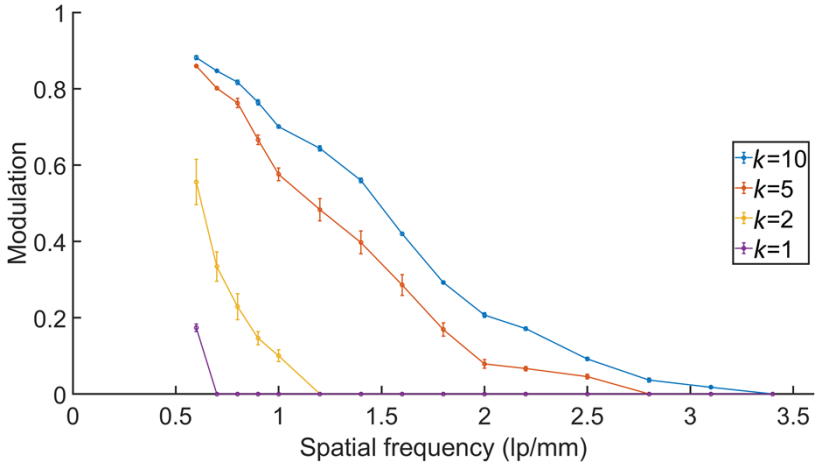

Fig. 8. The contrast transfer function (CTF) for optical sections constructed using upscaling factors where $k = 1, 2, 5, 10$; $u = 8$, and $S = 1.0$ mm (error bars; SE, $n = 5$). The data was collected using a line-pair phantom manufactured by Leeds Test Objects (Type 41-005).

Optics EXPRESS

A reduction in the total number of subshells (including a single subshell $u = 1$) had little impact on the trend of the CTF graphs shown in Fig. 8, apart from a marginal increase in SE. This is because additional subshells increase the mean number of samples contributing per constructed pixel (see Fig. 6), thereby enhancing the FF and eradicating nulls (especially important for high values of upscaling factor k, see Fig. 5) and does not change the resolution of the resultant section. The latter is set by k as previously discussed at the beginning of this section.

3.3. Optical sections from a complex phantom

In the second experiment, the core phantom was raster scanned similarly to the first. A series of (unpadded) oblique projections $M_{\gamma xy}(r)$ produced from pixels collected from a single subshell over a complete raster scan can be seen in the visualization of Fig. 9.

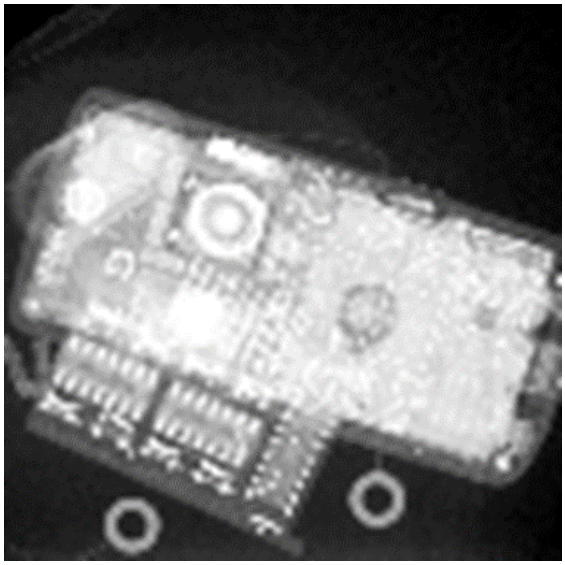

Fig. 9. A cropped (100^2 pixels) unpadded $k = 1$ oblique projection from the luggage core phantom comprising data from a single subshell $u = 1$, collected using a scan step of $S = 1.0$ mm. The full 'raw' projection series $M_{\gamma xy}(r)$ (where each projection comprises 141^2 pixels) can be seen in the video sequence of (Visualization 1) where the orbit diameter of image structures increases with increased separation from the source plane.

The construction of an optical section T_z, following Eqs. (1)–(9) at an axial focal plane position z is specified by calculating the appropriate shift $r(i)$ via Eq. (6). Similarly, a series of equally spaced sections can be specified via an incremental change δz, see Fig. 10 (Visualization 2). It can be appreciated that the in-plane (x,y) spatial fidelity of sections improved with increased upscaling as predicted by theory and the CTF measurements taken at $k = 1,2,3$, and 5. However, the native resolution of the detector/source system limited the benefit of upscaling above $k \sim 6$ as discussed in section 3.2. The marginal enhancement observed for $k = 10$ was attributed to the 'smoothing' due to the higher density pixilation of fine structures, see respectively Fig. 10 (e) and (f), but such effects did not consistently impact CTF analysis. In general, the image fidelity was entirely consistent with theory until bounded by the Nyquist limit and therefore, in good agreement with the CTF plots recorded in Fig. 8. Similar limitations applied to the section thickness $\delta t \propto S/k$ from Eq. (6), where for example, k and δt are, respectively, (1, 6.4 mm) and (5, 1.3 mm). Thus, axial steps of $\delta z < \delta t$ are associated with limited focusing over δt. While small

Optics EXPRESS

changes in image content were observable when $\delta z \ll \delta t$ this was primarily due to rounding changes in Eq (5).

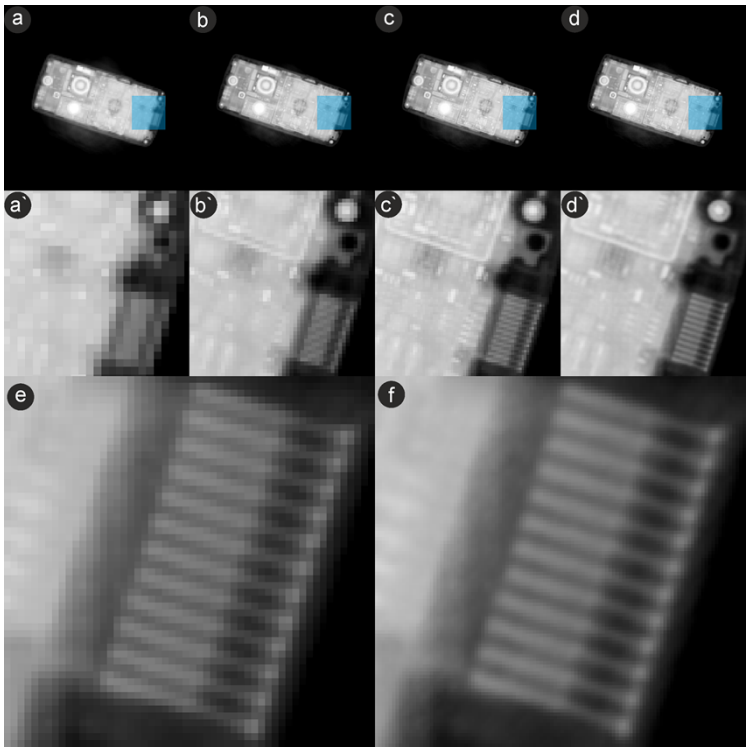

Fig. 10. Montage of zoomed optical sections of the mobile phone in the luggage core phantom highlighting improvements in image fidelity due to upscaling via null padding. All sections are constructed using projection data collected over a 140 mm square raster scan with a step size of $S = 1.0$ mm and an eight-shell beam $u = 8$. The upscaling factor k, upscaling ratio $\eta \times 100\%$, total number of pixels composing a section, and the approximate slice thickness δt, are as follows: (a-a') $k = 1$, 100%, 141^2 pixels, $\delta t \sim 6.4$ mm; (b-b') $k = 2$, 25.2%, 281^2 pixels, $\delta t \sim 3.2$ mm; (c-c') $k = 3$, 11.2%, 421^2 pixels, $\delta t \sim 2.1$ mm; (d-d') $k = 5$, 4.0%, 701^2 pixels, $\delta t \sim 1.3$ mm. A 'live' montage showing focusing and zooming can be seen in (Visualization 2) where the axial focal plane z-axis readout is implemented in $\delta z = 1$ mm steps i.e., the mean axial position of the slice. The pair of images at the bottom of the figure is of the mobile phone's charging port where (e) has the same parameters as (d-d'); and (f) $k = 10$, 1.0%, 1401^2 pixels, $\delta t \sim 0.65$ mm.

4. Conclusion

We have described in theory and validated empirically interleaved sampling for high resolution X-ray tomography using multiplexed conical subshells. Our new method combines enhanced spatial fidelity with a reduction in X-ray measurements, each being a very significant improvement in comparison to prior shell beam methods [35,36].

A five-fold increase in the CTF was recorded for optical sections constructed from projection data sampled on a 1 mm grid and upscaled by a factor of $k = 10$. The oblique projections comprised 1% sample pixels and 99% null pixels. However, the native resolution of the detector/source system limited the benefit of upscaling above $k \sim 6$. This result demonstrated that the native resolution of the image capture system is the fundamental limiting condition of our approach.

Optics EXPRESS

We have demonstrated periodic sampling of X-ray beam subshells to produce null upscaled oblique views. A pixel stream collected from a sampling point, on a single shell, over the raster scan produces an oblique projection. The relative registration of the upscaled projections form periodically sparse interleaved grids. The null padding ensures that sample pixels maintain their original sampling registration and via tomosynthesis maximize spatial resolution according to the Nyquist limit of the source/detector system. Novel mapping of the variable contributions across each section is incorporated into the tomosynthesis. Thus, our method is deterministic and does not require, for instance, interpolation or image cross-correlation as used in super-resolution. By hypothesis, in comparison to iterative algorithms our method has greater predictability of response in the presence of non-systematic noise. By similar reasoning, we expect the increase in CTF to be relatively robust in the presence of clutter encountered routinely in practical applications such as luggage screening.

While optimization of data acquisition was not the objective of this work, we can make a rough comparison with the earlier approaches. For example, to obtain a similar spatial resolution using the prior methods requires replacing each virtual sample point (represented by a null in the contribution map) with a real sample. Therefore, our new method for a given resolution and source/detector/scan parameterization, reduces the data acquisition requirement by around 2-orders of magnitude in comparison with our initial tomographic method [35], and around 1-order of magnitude for the sporadic tomography [36]. However, the non-equivalence between the sampling structures of each different approach would be expected to impact photon counting statistics per constructed pixel (x,y,z), and this aspect requires further systematic study. Nonetheless, a significant reduction in the total scan time does appear realistic.

Our work dovetails with recent advancements in flat-panel array sources, which can fire X-ray emitters in sequence or simultaneously without mechanical scanning. Also, the discrete distribution of the X-ray emission points complements our 'sampling grid' approach, see Fig. 2(a). These considerations scale positively with brighter sources and facilitate highspeed image capture. Thus, beyond the work detailed in this paper, there is considerable scope to optimize the data acquisition and scanning approach.

Such capability promises rapid operational speeds when combined with our method. Also, our theoretic analysis supports scalability in inspection space and does not impose limits on X-ray energy. We believe a combined approach has many potential applications in nondestructive evaluation and characterization, explosives and weapons detection, and medical imaging.

Funding. Royal Society Wolfson Fellowship (RSWF\R1\180012); Engineering and Physical Sciences Research Council (EP/T034238/1); U.S. Department of Homeland Security (HSHQDC-15-C-B0036).

Disclosures. The authors declare no conflicts of interest.

Data availability. Data underlying the results presented in this paper are not publicly available at this time but may be obtained from the authors upon reasonable request.

References

1. H. E. Martz, C. M. Logan, D. J. Schneberk, and P. J. Shull, *X-Ray Imaging: Fundamentals, Industrial Techniques and Applications* (Taylor and Francis, 2017).
2. M. E. Coles, "X-ray imaging," in *Experimental Methods in the Physical Sciences* (Elsevier,1999), Vol. 35, Chap. 8.
3. F. Adams, "X-ray absorption and diffraction-overview," in *Encyclopedia of Analytical Science* (Elsevier, 2005), pp.365–378.
4. S. P. Poplack, M. Bath, A. A. Johnsson, D. J. Godfrey, L. Ren, Q. Wu, and F. Yin, "Sect. V Clinical applications," in *Tomosynthesis Imaging* (Taylor and Francis, 2014), pp. 181–225.
5. E. Seeram, "Computed Tomography: Physical Principles," *Clinical Applications, and Quality Control*, 4th ed. (Elsevier, 2016).
6. G. Chen, "Understanding X-ray cargo imaging," in Nuclear Instruments and Methods in Physics Research, Section B: Beam Interactions with Materials and Atoms (2005), pp. 810–815.
7. K. Wells and D. A. Bradley, "A review of x-ray explosives detection techniques for checked baggage," Appl. Radiat. Isot. **70**(8), 1729–1746 (2012).
8. A. Mouton and T. P. Breckon, "A review of automated image understanding within 3D baggage computed tomography security screening," J. X-Ray Sci. Technol. **23**(5), 531–555 (2015).

Optics EXPRESS

9. T. W. Rogers, N. Jaccard, E. J. Morton, and L. D. Griffin, "Automated X-ray image analysis for cargo security: Critical review and future promise," J. X-Ray Sci. Technol. **25**(1), 33–56 (2017).
10. F. Xu, L. Helfen, T. Baumbach, and H. Suhonen, "Comparison of image quality in computed laminography and tomography," Opt. Express **20**(2), 794–806 (2012).
11. J. Vila-Comamala, L. Romano, K. Jefimovs, H. Dejea, A. Bonnin, A. C. Cook, I. Planinc, M. Cikes, Z. Wang, and M. Stampanoni, "High sensitivity X-ray phase contrast imaging by laboratory grating-based interferometry at high Talbot order geometry," Opt. Express **29**(2), 2049–2064 (2021).
12. G. Travish, F. J. Rangel, M. A. Evans, B. Hollister, and K. Schmiedehausen, "Addressable flat-panel x-ray sources for medical, security, and industrial applications," Proc. SPIE **8502**, 85020L (2012).
13. J. Park, J. Jung, A. P. Gupta, J. Soh, C. Jeong, J. Ahn, S. Cho, K. Yoon, D. Kim, M. Mativenga, and J. Ryu, "Multi-beam x-ray sources with carbon nanotube emitter for tomosynthesis system," Proc. SPIE **11312**, 113122E (2020).
14. S. Singh and M. Singh, "Explosives detection systems (EDS) for aviation security," Signal Proc. **83**(1), 31–55 (2003).
15. G. Harding, "X-ray diffraction imaging – a multi-generational perspective," Appl. Radiat. Isot. **67**(2), 287–295 (2009).
16. M. Hassan, J. A. Greenberg, I. Odinaka, and D. J. Brady, "Snapshot fan beam coded aperture coherent scatter tomography," Opt. Express **24**(16), 18277–18289 (2016).
17. C. K. Egan, S. D. M. Jacques, M. D. Wilson, M. C. Veale, P. Seller, A. M. Beale, R. A. D. Pattrick, P. J. Withers, and R. J. Cernik, "3D chemical imaging in the laboratory by hyperspectral X-ray computed tomography," Sci. Rep. **5**(1), 15979 (2015).
18. A. Shevchuk, J. P. O. Evans, A. J. Dicken, F. Elarnaut, D. Downes, S. X. Godber, and K. D. Rogers, "Combined X-ray diffraction and absorption tomography using a conical shell beam," Opt. Express **27**(15), 21092–21101 (2019).
19. J. Zhang, Y. Hu, J. Yang, Y. Chen, J. Coatrieux, and L. Luo, "Sparse-view X-ray CT reconstruction with Gamma regularization," Neurocomputing **230**, 251–269 (2017).
20. A. P. Cuadros and G. R. Arce, "Coded aperture optimization in compressive X-ray tomography: a gradient descent approach," Opt. Express **25**(20), 23833–23849 (2017).
21. P. Cuadros, C. Peitsch, H. Arguello, and G. R. Arce, "Coded aperture optimization for compressive X-ray tomosynthesis," Opt. Express **23**(25), 32788–32802 (2015).
22. Y. Kaganovsky, D. Li, A. Holmgren, H. Jeon, K. P. MacCabe, D. G. Politte, J. A. O'Sullivan, L. Carin, and D. J. Brady, "Compressed sampling strategies for tomography," J. Opt. Soc. Am. A **31**(7), 1369–1394 (2014).
23. T. Dreier, N. Peruzzi, U. Lundström, and M. Bech, "Improved resolution in x-ray tomography by super-resolution," Appl. Opt. **60**(20), 5783–5794 (2021).
24. K. Rogers and P. Evans, "X-ray diffraction and focal construct technology," in *X-Ray Diffraction Imaging: Technology and Applications*, J. Greenberg, ed. (Taylor and Francis, 2019), Chap. 6.
25. A. Dicken, J. P. O. Evans, K. D. Rogers, C. Greenwood, S. X. Godber, D. Prokopiou, N. Stone, J. G. Clement, I. Lyburn, R. M. Martin, and P. Zioupos, "Energy-dispersive X-ray diffraction using an annular beam," Opt. Express **23**(10), 13443–13454 (2015).
26. P. Evans, K. Rogers, J. Chan, J. Rogers, and A. Dicken, "High intensity X-ray diffraction in transmission mode employing an analog of Poisson's spot," Appl. Phys. Lett. **97**(20), 204101 (2010).
27. P. Evans, K. Rogers, A. Dicken, S. Godber, and D. Prokopiou, "X-ray diffraction tomography employing an annular beam," Opt. Express **22**(10), 11930–11944 (2014).
28. F. Li, Z. Liu, and T. Sun, "Annular beam high-intensity X-ray diffraction based on an ellipsoidal single-bounce monocapillary," J. Appl. Crystallogr. **49**(2), 627–631 (2016).
29. F. Li, Z. Liu, T. Sun, B. Jiang, and Y. Zhu, "Focal construct geometry for high intensity energy dispersive x-ray diffraction based on x-ray capillary optics," J. Chem. Phys. **144**(10), 104201 (2016).
30. D. Prokopiou, K. Rogers, P. Evans, S. Godber, and A. Dicken, "Discrimination of liquids by a focal construct X-ray diffraction geometry," Appl. Radiat. Isot. **77**, 160–165 (2013).
31. A. Dicken, J. P. O. Evans, K. D. Rogers, D. Prokopiou, S. X. Godber, and M. Wilson, "Depth resolved snapshot energy-dispersive X-ray diffraction using a conical shell beam," Opt. Express **25**(18), 21321–21328 (2017).
32. B. Ghammraoui, V. Rebuffel, J. Tabary, C. Paulus, L. Verger, and P. Duvauchelle, "Effect of grain size on stability of X-ray diffraction patterns used for threat detection," Nucl. Instrum. Methods Phys. Res., Sect. A **683**, 1–7 (2012).
33. D. Prokopiou, J. McGovern, G. Davies, S. Godber, P. Evans, A. Dicken, and K. Rogers, "A new parafocusing paradigm for X-ray diffraction," J. Appl. Crystallogr. **53**(4), 1073–1079 (2020).
34. A. Dicken, J. P. O. Evans, K. D. Rogers, D. Prokopiou, S. X. Godber, F. Elarnaut, A. Shevchuk, D. Downes, and M. Wilson, "Confocal energy-dispersive X-ray diffraction tomography employing a conical shell beam," Opt. Express **27**(14), 19834–19841 (2019).
35. J. P. O. Evans, S. X. Godber, F. Elarnaut, D. Downes, A. J. Dicken, and K. D. Rogers, "X-ray absorption tomography employing a conical shell beam," Opt. Express **24**(25), 29048–29059 (2016).
36. F. Elarnaut, J. P. O. Evans, D. Downes, A. J. Dicken, S. X. Godber, and K. D. Rogers, "Sporadic absorption tomography using a conical shell X-ray beam," Opt. Express **25**(26), 33029–33042 (2017).
37. Leeds Test Objects Medical Imaging Phantoms, "Resolution test patterns, star patterns, rulers: type 41-005," http://www.leedstestobjects.com/index.php/phantom/resolution-test-patterns/.

Optics EXPRESS

38. V. Kaftandjian, Y. M. Zhu, G. Roziere, G. Peix, and D. Babot, "A comparison of the ball, wire, edge, and bar/space pattern techniques for modulation transfer function measurements of linear x-ray detectors," J. X-Ray Sci. Technol. **6**(2), 205–221 (1996).